



Significance of grain refinement on micro-mechanical properties and structures of additively-manufactured CoCrFeNi high-entropy alloy

Wenrui Zhao^a, Jae-Kyung Han^a, Yulia O. Kuzminova^b, Stanislav A. Evlashin^b, Alexander P. Zhilyaev^{c,d}, Alexander M. Pesin^c, Jae-il Jang^e, Klaus-Dieter Liss^{f,g,c}, Megumi Kawasaki^{a,c,*}

^a School of Mechanical, Industrial and Manufacturing Engineering, Oregon State University, Corvallis, OR, 97331, USA

^b Center for Design, Manufacturing & Materials, Skolkovo Institute of Science and Technology, Moscow, 143026, Russia

^c Laboratory of Mechanics of Gradient Nanomaterials, Novos Magnitogorsk State Technical University, Magnitogorsk, 455000, Russia

^d Institute for Metals Superplasticity Problems, Ufa, 450001, Russia

^e Division of Materials Science and Engineering, Hanyang University, Seoul, 04763, Republic of Korea

^f Materials and Engineering Science Program, Guangdong Technion - Israel Institute of Technology, Shantou, Guangdong, 515063, China

^g Technion - Israel Institute of Technology, Haifa, 32000, Israel

ARTICLE INFO

Keywords:

Additive manufacturing
Grain refinement
High entropy alloy
Nanoindentation
X-ray diffraction

ABSTRACT

Grain refinement is an effective approach to improve mechanical properties of conventionally-manufactured high entropy alloys (HEAs). Additive manufacturing of HEAs is a new materials challenge and increasing reports are available for exploring the optimal processing parameters and post-manufacturing treatments to advance the physical and mechanical properties of additively-manufactured (AM) HEAs. At the current stage of the development of AM HEAs, it is necessary to investigate the significance of grain refinement on their mechanical properties and structures. In the present study, a CoCrFeNi HEA is manufactured by a laser powder-bed fusion technique using pre-alloyed HEA powders on which grain refinement was conducted by high-pressure torsion for up to 8 turns under 6 GPa at room temperature. The results from nanoindentation and Vickers microhardness testing demonstrate high strain hardening capability and increased plasticity, thus potentially high ductility, in the nanostructured AM CoCrFeNi HEA. X-ray diffraction analysis demonstrates the structural evolution with decreasing crystallite size, increasing microstrain and expanding lattice parameter with grain refinement in the HEA. The structural changes justify the estimation by nanoindentation of the rate-controlling mechanism of the grain boundary-mediated dislocation activity for the nanostructured AM HEA. This study provides advantages of nanostructuring for current developments in the AM technology of HEAs.

1. Introduction

A breakthrough of traditional alloy design involving a principle element with additions of minor elements was achieved by an introduction of high-entropy alloys (HEAs) having multiple principle elements with equiatomic or near equiatomic configurations that often lead to a simple crystalline structure [1–3]. Numerous research studies in the last decade described the superior mechanical properties of HEAs and their structural changes at a wide range of temperatures, and these intensive studies yielded several reviews in literature. Specifically, several reviews placed their special focuses on physical properties including magnetic, electrical and thermal properties [4], structure and

phase balance [5,6] and the thermodynamic concepts [7] of HEAs, while additional reviews focus more on general mechanical properties and deformation mechanisms [8,9] as well as fracture and magnetization [10] and corrosion resistance [11] of HEAs. Moreover, a recent report summarized the mechanical behavior of HEAs having heterogeneous microstructures [12].

Bulk HEAs have been produced by a conventionally-manufactured (CM) approach of melting and casting as well as solid-state techniques of mechanical alloying [13,14]. Thin film deposition and sputtering of HEAs are also developed for coating purposes [15,16]. Nevertheless, the majority of the research and applications use bulk HEAs and processing of nanocrystalline HEAs has become one of the major topics in the

* Corresponding author. School of Mechanical, Industrial and Manufacturing Engineering, Oregon State University, Corvallis, OR, 97331, USA.
E-mail address: megumi.kawasaki@oregonstate.edu (M. Kawasaki).

society. Applications of severe plastic deformation is a well-recognized procedure for processing of bulk nanocrystalline metals and alloys [17], and it was utilized for nanocrystallization of bulk HEAs. Specifically, as far as CM HEAs with an *f.c.c.* single phase or an *f.c.c.* major phase, equal-channel angular pressing (ECAP) was conducted on a CoCrFeNiMn alloy [18], and high-pressure torsion (HPT) was applied on CoCrFeNi alloy [19], CoCrFeNiMn alloys [20–28], $Al_{0.1-0.3}CoCrFeNi$ alloys [29,30] and a $(CoCuFeNi)_{1-x}Ti_xAl_x$ alloy [19]. Moreover, HPT was applied for sintering of mechanically-alloyed powders leading to an HPT-induced CoCrFeNiMn alloy [31]. Grain refinement at the surfaces of HEAs are reported by applying an ultrasonic surface mechanical attrition treatment (SMAT) on CM CoNiCrMn and FeCoNiCrMn–Al HEAs [32].

Additive manufacturing of HEAs is a new materials challenge and earlier representative studies were reported in 2015 [33,34]. Increasing reports are available in the last five years for exploring the optimal AM processing parameters to advance the physical and mechanical properties of additively-manufactured (AM) HEAs and the several summaries are published elsewhere [35–39]. Although advantages of high efficiency of additive manufacturing in the metal production processes attracted much attentions to AM HEAs, the post-treatments for surface hardening by laser shock peening on an AM CoCrFeMnNi alloy [40] and aerosol deposition on an AM $Fe_{40}(CoCrMnNi)_{60}$ alloy [41] reveal the necessity of post-manufacturing treatments in the current AM HEAs as well as the feasibility of grain refinement on cultivating the existing good mechanical properties in the AM HEAs.

Accordingly, at the current early stage of development in AM HEAs, it is indispensable to investigate the significance of grain refinement in bulk volume on mechanical properties and structural changes. The present study demonstrates an improved strain hardenability by Vickers microhardness and enhanced plasticity by nanoindentation, thereby a potential for exhibiting high ductilities, and the detailed structural changes at different processing stages of AM and grain refinement by X-ray diffraction analysis of an AM CoCrFeNi HEA prepared by a laser powder-bed fusion technique followed by HPT at room temperature. This study informs the importance of grain refinement in the current advancement for the AM technology of HEAs.

2. Materials and experimental procedure

The CoCrFeNi HEA powders with the atomic fractions of 24 at.% Co, 26 at.% Cr, 25 at.% Fe, and 25 at.% Ni were produced by the atomization spraying method leading to powders with spherical morphology [38, 42]. Additive manufacturing of the bulk CoCrFeNi HEA was conducted by the Powder Bed Fusion (PBF) technology with a laser heat source (PBF-L) using a metal 3D printer, Trumpf TruPrint 1000. The bar-shaped cylindrical samples were printed (or built), where the lengths of the bars of ~ 8.5 cm is along the build direction and a diameter of the cross-section is 12.0 mm. The applied parameters for the printing process were set at a laser power of 150 W, a laser speed of 600 mm/s, a laser spot diameter of 55 μ m, hatch spacing of 80 μ m, and a layer thickness of 20 μ m. The printing process was performed in an inert atmosphere (Ar) with a gas feed velocity of 2.5 m/s at a chamber pressure of 1 bar. The oxygen level was kept within 0.3 at.%. Detailed procedures of additive manufacturing for the HEA are described in an earlier study, where an average particle size of the HEA powders is 35–40 μ m [43]. For comparison purposes, a conventionally-manufactured (CM) cast $Co_{25}Cr_{25}Fe_{25}Ni_{25}$ HEA was prepared in this study. A billet of the CM CoCrFeNi HEA was produced by vacuum induction melting of the alloy components having purity of >99.9 wt% followed by drop-casting. The cast ingot was subjected to hot-rolling at 1050 °C with a thickness reduction ratio of 64% and then annealing at 1100 °C for 1 h to achieve a homogenized microstructure. An earlier study showed that the solutionized CM CoCrFeNi HEA has an average grain size of $\sim 57 \pm 20$ μ m [26].

The prepared bars of the AM CoCrFeNi HEA were machined to have a

cross-section diameter of 10 mm and sliced into disks with thicknesses of ~ 0.85 mm by wire-cut electrical discharge machining. A set of disks was polished down to have final parallel thicknesses of ~ 0.83 mm and processed by HPT under quasi-constrained conditions at room temperature. The disks were processed under a compressive pressure of 6.0 GPa and a rotational speed of 1 rpm for total numbers of revolution, N , of 1/2, 1, 2, 4 and 8 turns for the AM HEA samples. These HPT-processed disks were cut into halves along the diameters and these were mold for polishing their vertical cross-sections. The surfaces were mechanically polished with 0.5 μ m alumina powders with ethanol and 0.05 μ m silica suspension to obtain mirror-like surfaces. Consistent sample preparations were applied for the CM HEA and the sample was processed for 1/2 and 5 HPT turns.

Vickers microhardness measurements were conducted to profile the hardness variations along the disk diameters on the polished vertical cross-sections of both CoCrFeNi HEA before and after HPT. The Vickers microhardness values, H_V , were recorded using a Mitutoyo HM-200 with an applied load of 100 gf and a dwell time of 10 s. The structural evolution of the AM HEA was examined at the conditions of initial powders, as-built without HPT and after HPT processing by X-ray powder diffraction (XRD) employing a Bruker D8 ADVANCE, using $Cu K_{\alpha}$ radiation at an incremental time of 3.0 s and a step size of 0.005° on slightly polished disk surfaces.

Microstructural examinations were conducted using scanning electron microscopy (SEM) for the AM HEA in an as-built condition and using transmission electron microscopy (TEM) after HPT processing. An as-built surface vertical to the building direction of the AM CoCrFeNi HEA was mechanically polished with 40 nm silica suspension followed by electrochemical polishing in an electrolyte of 900 ml of butanol C_4H_9OH + 100 ml of perchloric acid $HClO_4$ at room temperature. SEM analysis was conducted using Carl Zeiss Supra 40. The TEM observations were conducted by high resolution TEM, HRTEM-Philips CM200 and Philips C2100, at an accelerating voltage of 200 kV. Conventional mechanical polishing was applied to prepare the TEM samples. The AM HEA after HPT was first cut and then ground to a thickness of lower than 100 μ m using grade 1000 abrasive paper. A series of 3 mm disks were punched out at r of ~ 3.5 mm in each disk sample, where r is the radius from the disk center. Using diamond paste, the punched samples were then polished and ion milled for thinning in the final step.

The micro-mechanical properties were examined at the disk edges of the AM and CM CoCrFeNi HEA before after HPT using a nanoindentation facility, Nanoindenter-XP, with a three-sided pyramidal Berkovich indenter having a center-line-to-face angle of 65.3° . More than 15 indentations were conducted at each testing condition for all samples to achieve statistically valid data. All measurements were conducted under a predetermined maximum applied load of $P_{max} = 50$ mN at constant indentation strain rates, $\dot{\epsilon}_i$, of 0.0125, 0.025, 0.05, and $0.1 s^{-1}$, which are equivalent to general strain rates, $\dot{\epsilon}$, of 1.25×10^{-4} , 2.5×10^{-4} , 5.0×10^{-4} , and $1.0 \times 10^{-3} s^{-1}$, respectively, by taking account of the empirical relation of $\dot{\epsilon} \approx 0.01 \dot{\epsilon}_i$ [44].

3. Experimental results

3.1. Hardness development

Fig. 1 shows the Vickers microhardness distributions along the radius of the disks of (a) AM HEA and (b) CM HEA before and after HPT processing. The plots represent the hardness variations over the disk surfaces, since, as defined by the principles of HPT processing [45], the evolution of hardness is generally with radial symmetry in the HPT-processed disks. The dashed horizontal line in each plot denotes the initial average hardness value of $H_V \approx 260$ and ~ 160 for the AM and CM CoCrFeNi HEA, respectively. These measured hardness values in the present study are in a reasonable range with the reported values of $H_V = 238$ and 118 for a CoCrFeNi HEA manufactured by a powder-bed AM technique and a CM technique by casting, respectively [34]. A higher

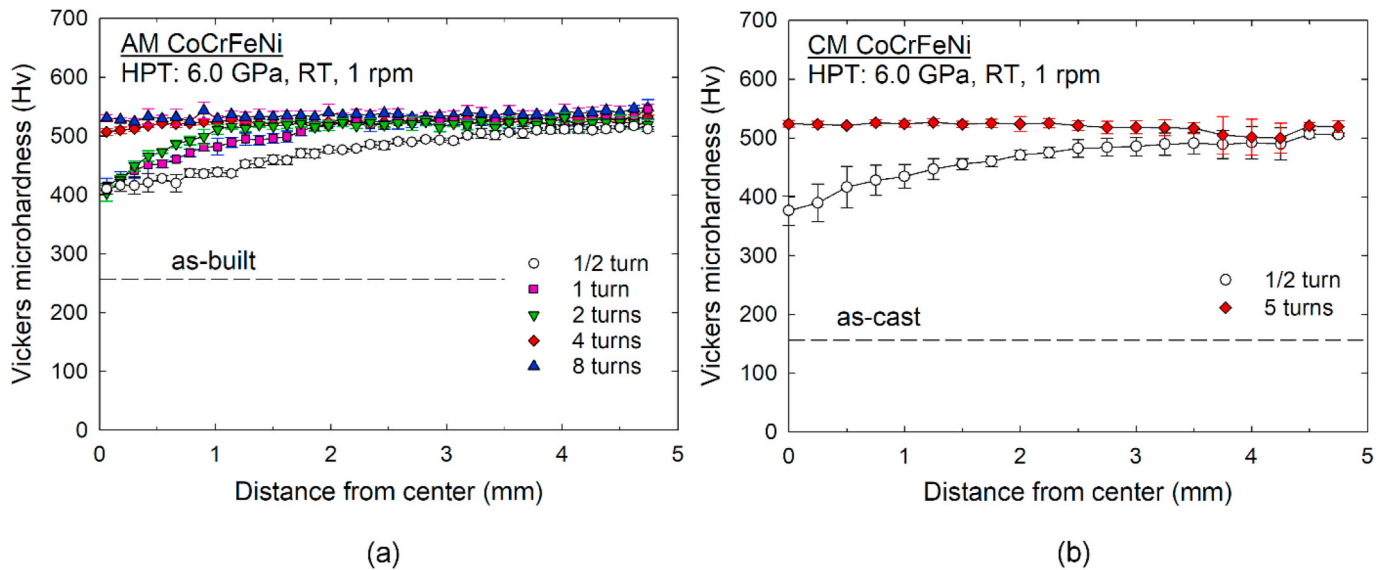


Fig. 1. Vickers microhardness distributions along the radius of the disks of (a) AM CoCrFeNi HEA and (b) CM CoCrFeNi HEA before and after HPT processing.

hardness of the AM HEA than the CM HEA is attributed to the different microstructures introduced by the different processing routes. The result is in good agreement with an earlier report demonstrating significantly higher yield strengths of ~ 500 – 510 MPa in an as-built CoCrFeNiMn alloy through selective laser melting with different laser scanning speeds than ~ 200 MPa for the as-cast CoCrFeNiMn alloy [46]. The high strength in the as-built alloy was attributed to the processing procedure enabling the formation of hierarchical cellular microstructure that led to a large contribution to dislocation strengthening.

The AM HEA shows a significant hardness increase to $H_V = 400$ at the center of the disk after 1/2 turn by HPT and the hardness gradually increases to ~ 510 towards the disk edge as shown in Fig. 1(a). Increasing numbers of HPT turns to 1 and 2, the central region of the disk having low hardness shrinks and the region with high hardness of $H_V = 525$ extends at $r > 2.0$ mm. Ultimately, the hardness value reaches saturation at $H_V = 525$ throughout the disk diameter after 4 and 8 HPT turns of grain refinement. A consistent trend of hardness evolution was observed in the CM HEA after HPT for 1/2 turn as shown in Fig. 1(b), where the hardness value increases to $H_V = 375$ at the disk center and further increases to 500 towards the disk edge. Homogeneously distributed high hardness of $H_V = 525$ in saturation was observed across the disk radius after 5 HPT turns. The results suggest that the CoCrFeNi HEA manufactured by the different procedures enable the demonstration of a consistent upper hardness limit at $H_V = 525$ after severe deformation by sufficient HPT turns of over 4–5. It should be noted that a hot-isostatic processed $\text{Al}_{0.1}\text{CoCrFeNi}$ alloy after mechanical alloying of powders processed by HPT for 2 turns showed a significant increase in hardness from $H_V = 135$ to 482 [30]. Moreover, reasonably similar high hardness was proclaimed in several CM HEAs having an *f.c.c.* crystal structure after HPT: an $\text{Al}_{0.3}\text{CoCrFeNi}$ alloy ($H_V \approx 530$ after 8 turns [29]), CoCrNiFeMn alloys ($H_V \approx 520$ after 5 turns [20], 486 ± 15 at the disk edge after 2 turns [21], and 450 after 10 turns [22]), and a $(\text{FeNiCoCu})_{86}\text{Ti}_7\text{Al}_7$ alloy ($H_V = 525$ after 10 turns [19]).

3.2. Microstructural evolution

Fig. 2 shows the XRD patterns measured at the overall mid-thickness disk surfaces of the AM CoCrFeNi HEA disks in the conditions of, from top, atomized powders, as-built, and after HPT for 1/2, 1, 2, 4, and 8 turns. There are three notable features in Fig. 2. First, all major peaks in each sample condition are determined as a pure *f.c.c.* structure, such as 111, 200, 220, 311, and 222 (indexed in red), thereby implying a

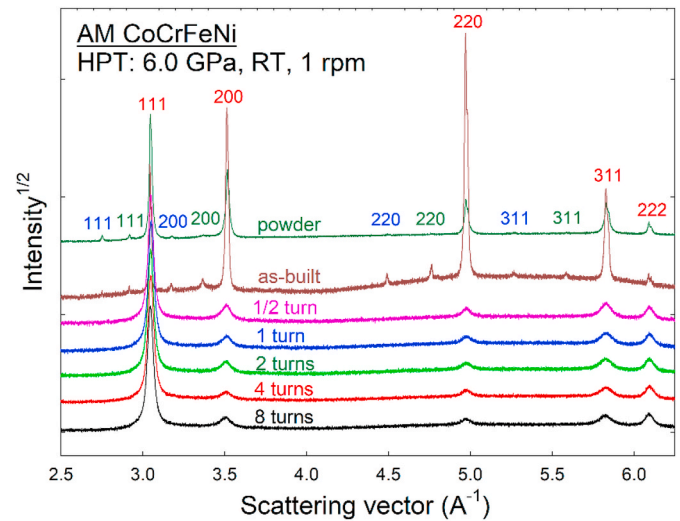


Fig. 2. XRD patterns taken at overall disk surfaces at the mid-thickness of the CoCrFeNi HEA disks in the conditions of, from the top, atomized powders, as-built, and after HPT for 1/2, 1, 2, 4, 8 turns.

presence of an *f.c.c.* primary phase. Second, two additional sets of weak *f.c.c.* peaks (noted in blue and green) are detected for the CoCrFeNi HEA in powders and an as-built condition, whereas there remains only the *f.c.c.* primary phase in the HEA after HPT processing. Due to the weak relative intensity of the additional sets of the *f.c.c.* peaks, it is estimated that the volume fractions of these minor *f.c.c.* phases are close to the detection limit of XRD of ~ 5 vol.%. Peak position analysis provided the lattice parameters of $a = 3.572$ Å for the primary *f.c.c.* phase and 3.729 Å and 3.954 Å for the two minor *f.c.c.* phases with peaks indexed in green and blue, respectively, for the HEA in a powder condition. The measured lattice parameters for the minor *f.c.c.* phases confirm these are neither the commonly observed phases, such as *b.c.c.* phase and σ phase involving Cr, for the *f.c.c.* CoCrFeNi-based HEAs manufactured by mechanical alloying and sintering at 600–900°C [47,48] nor any possible oxides. A possibility of the additional *f.c.c.* phases may be attributed to the heterogeneous distributions of the HEA elements in powders and an as-built condition, where non-equimolar CoCrFeNi-based HEAs show variations in lattice parameter from $a = 3.58$ Å for equimolar CoCrFeNi-based HEAs [27,49,50]. Third, there is apparent peak

broadening after HPT in each major *f.c.c.* peak in comparison with those for the powders and as-built HEA indicating a refined crystallite size with defects. The peak broadening becomes further augmented with increasing numbers of HPT turns.

Fig. 3 shows representative backscattered electron (BSE) images in (a) low and (b) high magnifications of the as-built sample, and the TEM bright-field images of the AM CoCrFeNi alloy after HPT for (c) 1 turn and (d) 8 turns. These BSE micrographs were taken on the sample surfaces normal to the building direction. The TEM images include the corresponding selected-area diffraction (SAED) patterns. It is apparent from Fig. 3(a) that there is a duplex microstructure consisting of the elongated phases with 50–55 μm lengths which are associated with the laser spot diameter. Between the neighboring tracks, nearly equiaxed microstructures having a phase size of $<10\ \mu\text{m}$ is observed and it is due to the overlaps of the neighboring laser tracks leading to re-melting and recrystallization of the as-built phase. A typical granular configuration in the as-built materials is displayed with cellular sizes of $\sim 1.0\ \mu\text{m}$ as shown in Fig. 3(b). The observed as-built microstructure is well consistent with that of the Cantor alloy manufactured by the laser additive manufacturing methods [39].

The TEM micrographs describe the significant grain refinement in the microstructure of the AM HEA by severe plastic deformation. In practice, the grains are reasonably equiaxed even after 1 HPT turn in Fig. 3(c) and the ultrafine-grained microstructure continues through 8 HPT turns in Fig. 3(d), while the severe deformation introduces many dislocations around grain boundaries. The estimated average spatial grain sizes of the HEA are $d \approx 105\ \text{nm}$ and $\sim 90\ \text{nm}$ after 1 and 8 turns, respectively. The TEM observation was conducted at $r \approx 3.5\ \text{mm}$, and it is reasonable to conclude that the microstructure was severely refined and saturated at $r \approx 3.5\ \text{mm}$ even after 1 HPT turn. The result is fully consistent with the saturated Vickers microhardness value after 1 turn at $r \approx 3.5\ \text{mm}$ as shown in Fig. 1(a). The SAED patterns for both 1 and 8 turns confirm the presence of a single *f.c.c.* phase within the inspected regions. It should be noted that the observed ultrafine grain sizes of the

AM HEA are in good agreement with the earlier study showing $d \approx 77 \pm 31$, $\sim 46 \pm 16$, and $\sim 45 \pm 15\ \text{nm}$ after 1/4, 2 and 5 HPT turns, respectively, for the CM CoCrFeNi HEA [4], and the agreement in grain size is resulted in the consistent saturation hardness in the CoCrFeNi HEA as was shown in Fig. 1(a) and (b). It is worth noting that, while the current processing pressure of 6 GPa failed to show phase transformation in the *f.c.c.* CoCrFeNi HEA, an *f.c.c.* CoCrFeNiMn HEA starts to demonstrate *f.c.c.*-to-*h.c.p.* transformations under a high pressure of 14 GPa [51], while the *f.c.c.*-to-*h.c.p.* transition is sluggish in aluminum requiring $\sim 50\ \text{GPa}$ pressure [52].

3.3. Micro-mechanical properties of HEA

Nanoindentation was applied to investigate the micro-mechanical properties at the disk edges of the AM HEA in an as-built condition and after HPT for 8 turns and of the CM HEA after HPT for 5 turns. Nanoindentation is an advantageous technique to acquire the mechanical properties from small sample volumes, and it is beneficial to utilize the technique for small bulk samples including the HPT-processed disks [53]. Nanoindentation is even utilized for the advancement of CM HEAs [23,54]. Fig. 4 shows the representative load-displacement curves measured at four equivalent strain rates from 1.25×10^{-4} to $1.0 \times 10^{-3}\ \text{s}^{-1}$ at the disk edges of (a) the AM sample in an as-built condition and after HPT for 8 turns and (b) the CM HEA after HPT for 5 turns. Each curve is the average of at least 15 separate measurements.

The AM HEA after HPT for 8 turns shows smaller displacements than the HEA in an as-built condition at all strain rates as shown in Fig. 4(a). Thus, the AM HEA after grain refinement demonstrated higher hardness than the as-built HEA. Closer observation shows that the displacements are reasonably similar for both AM and CM HEA after HPT at all strain rates. The result indicates the consistent strength at each indentation strain rate and it is in an excellent agreement with the results from Vickers microhardness testing. All samples in Fig. 4(a) and (b) show positive strain rate dependency before and after grain refinement.

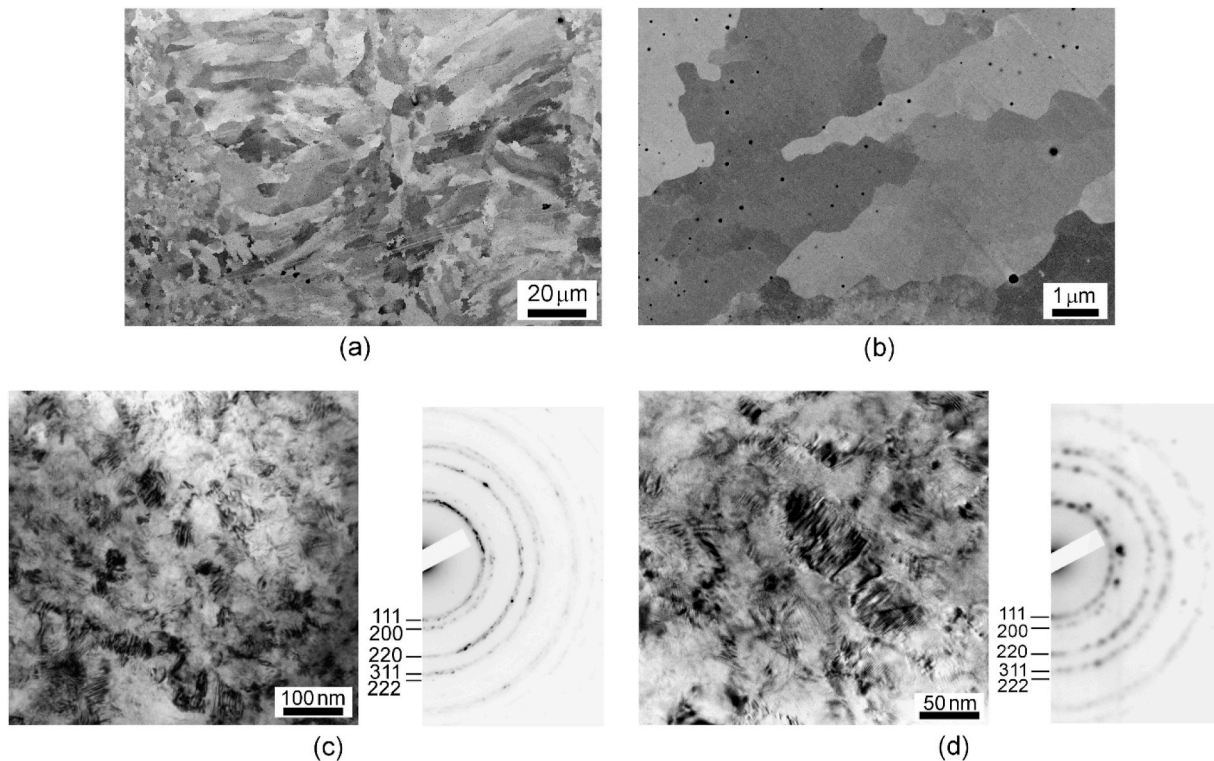


Fig. 3. Representative backscattered electron images in (a) low and (b) high magnifications of the as-built sample, and the TEM bright-field images of the AM CoCrFeNi alloy after HPT for (c) 1 turn and (d) 8 turns by HPT.

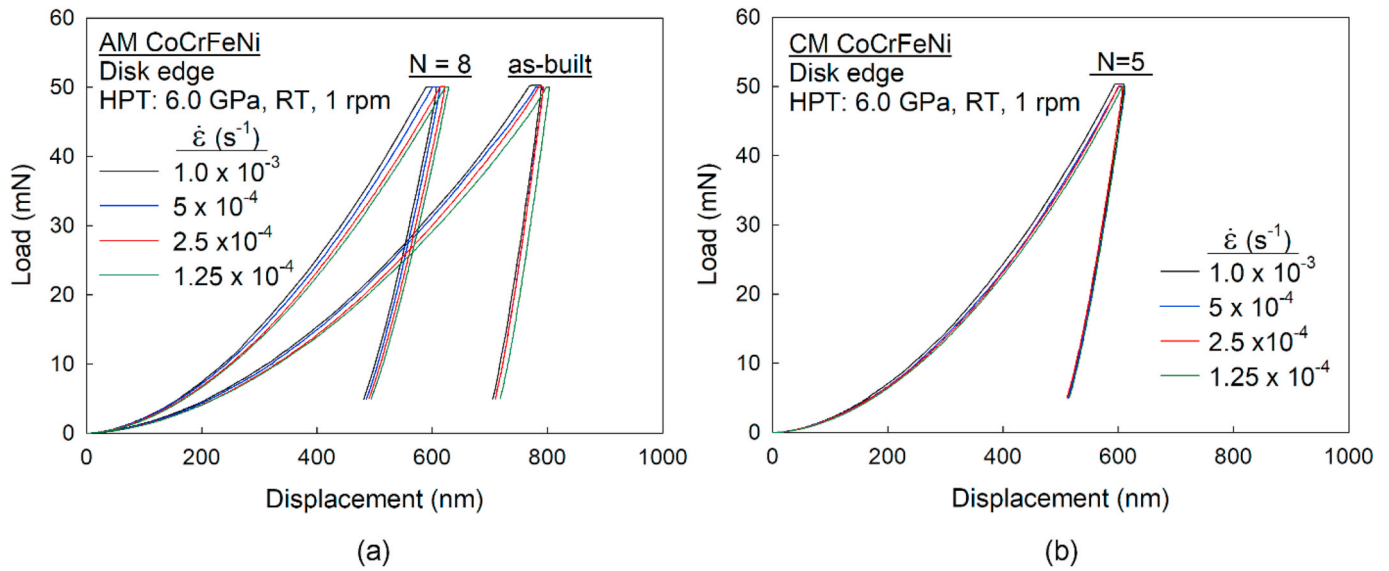


Fig. 4. Representative load-displacement curves measured at four equivalent strain rates from 1.25×10^{-4} to $1.0 \times 10^{-3} \text{ s}^{-1}$ at the disk edges of (a) AM sample in an as-built condition and after HPT for 8 turns and (b) CM HEA after HPT for 5 turns.

4. Discussion

4.1. Strain hardening of an AM CoCrFeNi HEA

A hardness increase in polycrystalline materials can be well defined by the Hall-Petch relationship [55,56], and the relationship between grain refinement and hardness was demonstrated earlier for a CM CoCrFeNiMn HEA after HPT up to 2 turns [21]. Specifically, severe torsion straining enabled the activation of atomic diffusion in the CoCrFeNiMn HEA leading to the significant microstructural evolution, while HEAs are well known for their sluggish diffusion [6,57]. Thus, it is anticipated that the microstructural refinement provides a major contribution to an increase in hardness of the present AM CoCrFeNi HEA. In order to understand the hardening behavior of the HEA during grain refinement processing, it is indispensable to apply an approach considering the equivalent strain introduced during HPT processing, $\epsilon_{\text{eq}} = 2\pi Nr/(\sqrt{3}h)$ [45] where h is the thickness of the disk sample. In the present analysis, $h = 0.7 \text{ mm}$ was applied since a small volume of the material flows out under the quasi-constrained HPT set-up during compression and an early torsional stage, thereafter it remains reasonably constant up to 8 turns by HPT.

Fig. 5 shows the relationship between Vickers microhardness and the equivalent strain for the AM HEA after HPT through 8 turns. It is apparent that the hardness drastically increases with increasing equivalent strain in an early stage of HPT up to $\epsilon_{\text{eq}} \approx 12$, thereafter the hardness becomes saturated at the maximum hardness of $H_V = 525$. Such hardness evolution with increasing equivalent strain is defined as a model of strain hardening without recovery during severe plastic deformation [58]. Although the plot is not shown, the CM HEA demonstrated the consistent hardness behavior. It should be emphasized that an equivalent strain of ~ 12 leading to the upper limit of the saturation hardness is consistent in both AM and CM HEA, while these have different processing routes that cause different initial hardness before HPT.

Further inspection of strain hardening behavior during deformation was conducted quantitatively by estimating the extent of strain hardening through the computation of the hardenability exponent, η . Thus, a linear plot showing hardness versus equivalent strain in Fig. 5 was replotted into a double-natural logarithmic plot and it is shown in Fig. 6 for (a) AM HEA and (b) CM HEA after HPT. The red and blue dotted trend lines describe two separate stages of the hardness developments

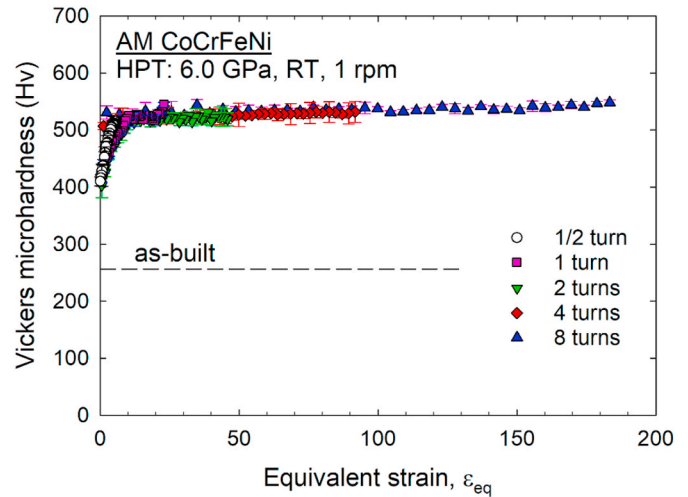


Fig. 5. Plot showing a relationship between Vickers microhardness and the equivalent strain for the AM HEA after HPT through 8 turns.

during grain refinement, and the values of η represent the slopes of those trend lines in the double-natural logarithmic plots. The transitions of strain hardening behaviors where the red and blue dotted lines intersect occur at $\ln(\epsilon_{\text{eq}}) \approx 2.5$, thus $\epsilon_{\text{eq}} \approx 12$, for both HEA. Considering the plots shown in Fig. 5, there is a significant hardness increase with high strain hardening up to $\epsilon_{\text{eq}} \approx 12$.

The red dashed lines in Fig. 6(a) and (b) enable quantitative expressions of strain hardening in the early stage of deformation towards grain refinement. The present CoCrFeNi alloy demonstrated reasonably similar values of strain hardening exponent of $\eta = 0.0859$ and 0.0871 in the AM and CM conditions, respectively, indicating that the processing of the starting material is less relevant in this stage of deformation. It is reasonable to note that a limited number of earlier reports demonstrate the strain hardening exponents of $\eta = 0.08$ for an AZ31 Mg alloy [59], $\eta = 0.07$ for a ZK60 Mg alloy [60], $\eta = 0.031$ for an Ti-6Al-4V alloy [61], and $\eta = 0.017$ for a Zn-3Mg alloy [62] after HPT for $\epsilon_{\text{eq}} < 20$ that is equivalent to $\ln(\epsilon_{\text{eq}}) < 3.0$. Thus, it is apparent with comparing these reference values that the present HEAs demonstrate significantly high η , thereby exhibiting the high hardenability in an early stage of

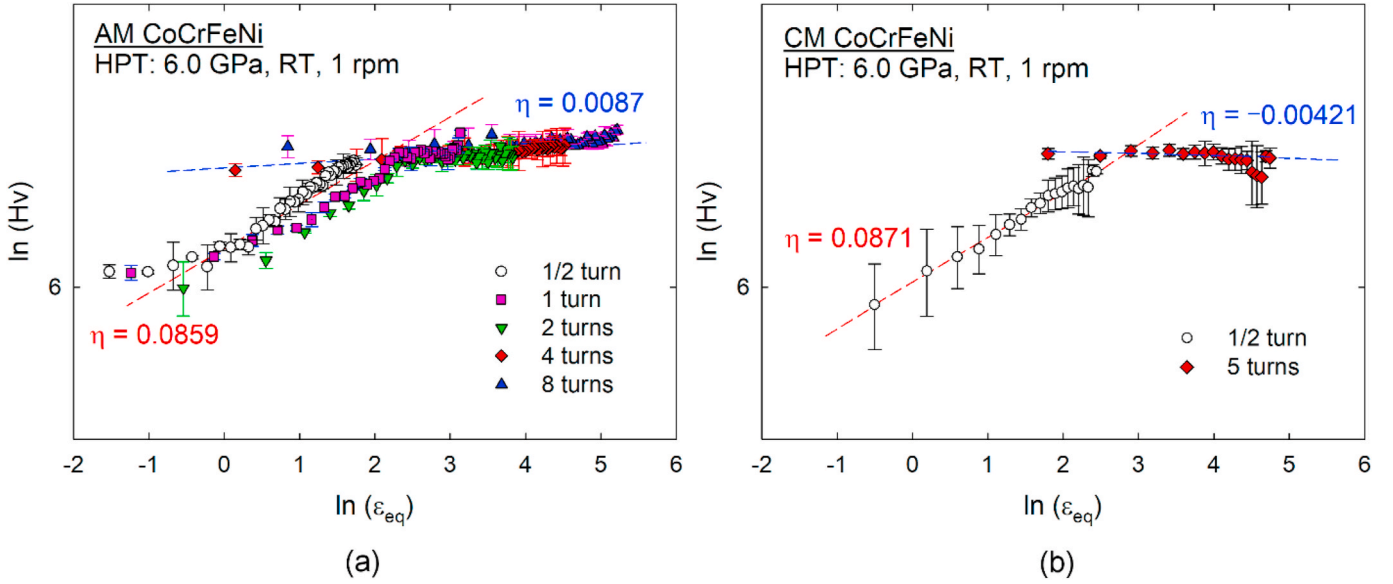


Fig. 6. Double-natural logarithmic plots of hardness versus equivalent strain for (a) AM HEA and (b) CM HEA after HPT.

deformation.

The hardness evolution tends to be stable beyond $\varepsilon_{eq} \approx 12$ according to the hardness measurements in Figs. 1 and 5, but it is notable with this analysis that the AM HEA show a positive strain hardening exponent of $\eta = 0.0087$ at the stable hardness evolution stage, while the CM HEA shows a negative value of $\eta = -0.0042$. It provides an excellent demonstration of the improved strain hardenability under plastic deformation with grain refinement in the AM CoCrFeNi HEA.

4.2. Micro-mechanical properties of an AM CoCrFeNi HEA

The load-displacement curves obtained through nanoindentation are used to analyze two important characteristics of materials, strain rate sensitivity, m , and the activation volume, V^* . Although the measurements were conducted at the disk edges, the hardness homogeneity was achieved after HPT for high numbers of turns as seen in Fig. 1 and it is reasonable to assume that the nanoindentation results represent the mechanical properties of the entire disk volumes of the HEA.

The value of m is calculated at a given strain, ε , and absolute temperature, T , by estimating the uniaxial flow stress, σ_f by Tabor's empirical relation of $\sigma_f \approx H/C$ where C is a constrain factor of ~ 3 for fully plastic deformation at constant strain rates, $\dot{\varepsilon}$ [63] and H is the nanoindentation hardness estimated according to the Oliver-Pharr method [64],

$$m = \left(\frac{\partial \ln \sigma_f}{\partial \ln \dot{\varepsilon}} \right)_{\varepsilon, T} = \left(\frac{\partial \ln(H/3)}{\partial \ln \dot{\varepsilon}} \right)_{\varepsilon, T} \quad (1)$$

Thus, the value of m is estimated from the slope of a double logarithmic plot of $H/3$ vs. $\dot{\varepsilon}$. The activation volume, V^* , is calculated by the following equation,

$$V^* = \sqrt{3}kT \left(\frac{\partial \ln \dot{\varepsilon}}{\partial \sigma_f} \right)_{\varepsilon, T} = \sqrt{3}kT \left(\frac{\partial \ln \dot{\varepsilon}}{\partial (H/3)} \right)_{\varepsilon, T} \quad (2)$$

where k is Boltzmann's constant.

Fig. 7 shows a double logarithmic plot of $H/3$ vs. $\dot{\varepsilon}$ for the AM HEA in an as-built condition and after HPT for 8 turns. The results for the CM HEA in an as-cast condition [26] and after HPT for 5 turns were shown together for comparison purposes. It is apparent that the m values improved from 0.046 to 0.058 by grain refinement in the AM HEA. The same trend is seen in the CM HEA with m values of 0.026 [26] and 0.031 before and after HPT, respectively, while the values for the CM HEA are

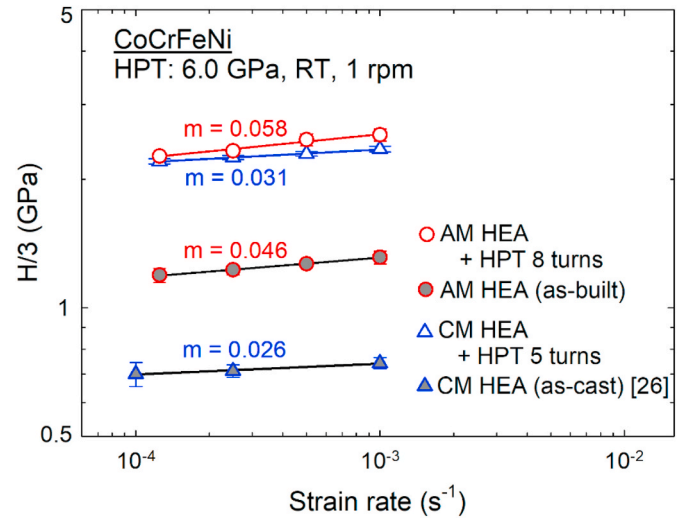


Fig. 7. Double logarithmic plot of $H/3$ vs. $\dot{\varepsilon}$ for the AM HEA in an as-built condition before HPT and after HPT for 8 turns. The results for the CM HEA in an as-cast condition [26] and after HPT for 5 turns were shown together.

lower and the improvement in m is less apparent than the AM samples. The reason may be attributed to the different manufacturing routes leading to the divergent initial bulk structures of the HEA before grain refinement by HPT, and it requires further experiments to identify the reason. Nevertheless, the improved strain rate sensitivity as well as the improved strain hardening capability discussed in an earlier section imply the significant potential of demonstrating high ductility in the AM HEA after grain refinement via HPT, while the HEA exhibits excellent hardness and strength.

It should be noted that the computed m values for both AM and CM CoCrFeNi HEA are valid according to the recent reports estimating the m values for CoCrFeNi alloys as $m = 0.044$ after production by induction melting having a grain size of $21.84 \mu\text{m}$ [65] and as $m = 0.068$ after manufacturing by magnetron sputtering having a crystallite size of $\sim 7.8 \text{ nm}$ [66]. Moreover, several *f.c.c.* HEAs demonstrate the m values between 0.02 and 0.07 [67]. The present AM HEA alloy before grain refinement demonstrates over one order of magnitude higher m value than simple coarse-grained *f.c.c.* metals, such as pure Ni showing $m \approx$

0.0028 [68]. Nevertheless, these simple *f.c.c.* metals increases strain rate sensitivity significantly with grain refinement [52,69] and the present HEAs follow the trend of simple *f.c.c.* metals by increasing *m* values with grain refinement.

The estimated activation volumes are $V^* = 7.64b^3$ and $3.20b^3$ for the AM HEA in an as-built condition and after HPT for 8 turns, respectively, where *b* is the Burgers vector and was calculated by $b = a_0 \times \sqrt{2} / 2 \approx 2.25 \times 10^{-10} m$ with applying the lattice parameter, a_0 , of 3.57 Å for the present HEA powders measured by XRD as well as the reported value for a CoCrFeNi alloy [50,70]. The same way of calculation yielded $V^* = 20.0b^3$ and $6.22b^3$ for the CM CoCrFeNi alloy before and after processing for 5 HPT turns, respectively. Earlier reports discuss the values of V^* vary by three orders of magnitude from $\sim 1b^3$ to $1000b^3$ depending on the different rate-limiting deformation processes of crystalline materials [71–73]. There is a report discussing the chemical short-range ordering of Cr in the atomic structure of HEAs [74], and such ordering may further contribute to the high friction stress in the HEA leading to an influence on the thermal activated process, thereby lowering the V^* value of the HEA in comparison with the defined values for the general *f.c.c.* metals. It is currently under debate in the estimation of V^* and its correlation with *m* for HEAs [67]. Nevertheless, the V^* values for the nanostructured HEA are in a vicinity of $\sim 10b^3$ in the present study and it is anticipated that the deformation mechanism is by grain boundary-mediated dislocation activity.

4.3. Structural evolution during grain refinement

The XRD line profiles were analyzed by applying the Williamson-Hall method for evaluating the structural changes in the AM HEA during additive manufacturing and grain refinement. A Williamson-Hall plot is shown in Fig. 8 where the full width at half maximum (FWHM), ΔQ , of the XRD peak profiles are plotted against the scattering vector, *Q*. Thus, microstrain, $\epsilon = \Delta Q/Q$, and the crystallite size are calculated from the slope and the reciprocal of y-intercept at $Q = 0$ of the fitted line,

respectively [75], for each sample condition. In this procedure, the selected X-ray diffraction data from the available close-packed family planes of 111 and 222 at $Q = 3.05$ and 6.09 \AA^{-1} were selected for the samples after grain refinement, so that the coherent crystallite sizes can be estimated by ignoring the smaller coherent sizes yielding larger peak broadening at the out-of-close-packed-plane coordinates of 200, 220 and 311 appearing at $Q = 3.50, 4.97$ and 5.82 \AA^{-1} . The latter reveal much wider peaks than the linear regression for the close-packed plane coordinates in each sample condition, disclosing significantly reduced coherent crystal sizes and larger strain gradients in those directions. Moreover, the larger broadening of the 200, 220 and 311 peaks for the HPT-processed material testify to reduced coherent crystal sizes due to interception by dislocations and planar faulting, which is consistent with the postulate of large numbers of dislocations showing grain boundary-mediated dislocation activity as the deformation mechanism of the nanocrystalline AM HEA. Four plane coordinates of 111, 200, 220, and 311 are used for the powder and as-built samples.

The estimated crystallite size and micro-strain are summarized in Table 1 for the AM CoCrFeNi in powders, as-built, and after HPT for up to 8 turns. The crystallite size of ~ 460 nm in powders increased to ~ 650 nm after the AM process, and it is influenced by the manufacturing

Table 1

Summary of estimated crystallite size, microstrain and lattice parameters for the AM CoCrFeNi HEA in the conditions of powders, and after additive manufacturing and HPT for up to 8 turns.

	Crystallite size (nm)	Microstrain	Lattice constant (Å)
Powder	462.54	0.00495	3.5718 ± 0.0007
As-built	652.27	0.00410	3.5744 ± 0.0009
HPT: 1/2 turn	101.25	0.00810	3.5742 ± 0.0048
HPT: 1 turn	116.11	0.00881	3.5728 ± 0.0051
HPT: 2 turns	80.94	0.00858	3.5752 ± 0.0059
HPT: 4 turns	89.65	0.00878	3.5745 ± 0.0059
HPT: 8 turns	75.07	0.00834	3.5771 ± 0.0069

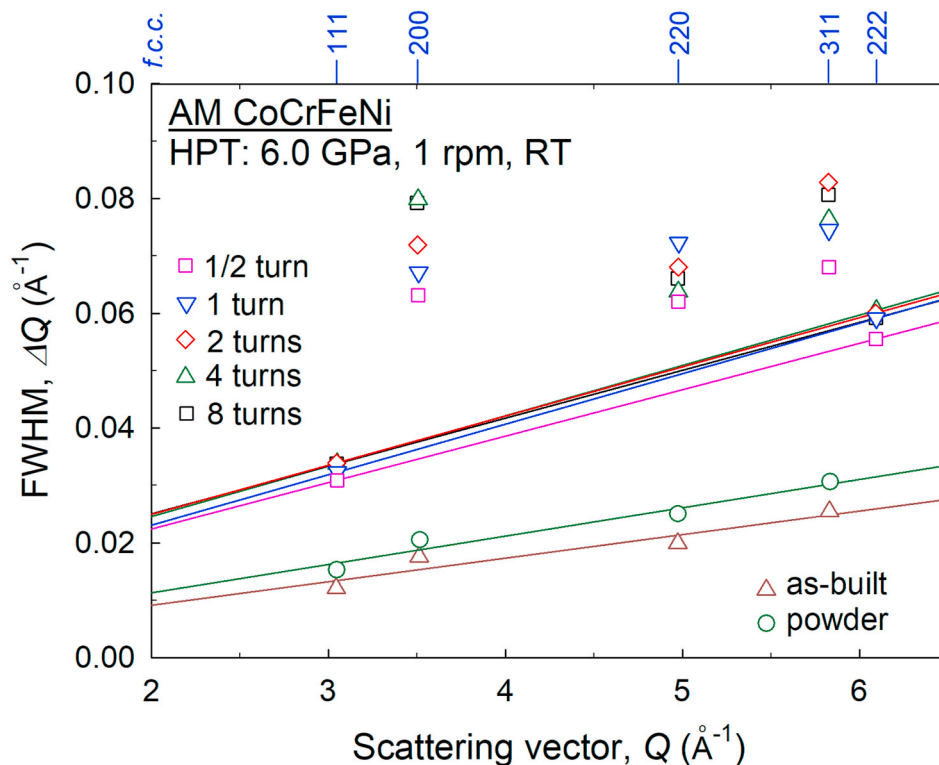


Fig. 8. A Williamson-Hall plot: the full width at half maximum (FWHM), ΔQ , of the XRD peak profiles against the scattering vector, *Q*, for the AM CoCrFeNi HEA the conditions of atomized powders, as-built, and after HPT for 1/2, 1, 2, 4 and 8 turns.

process involving lowered dislocation density through remelting, recovery and recrystallization at some local regions having the equiaxed phase structure as shown in Fig. 3(a) and (b). Such change in microstructure is consistent with the decreased microstrain from 0.00495 in powders to 0.00410 after printing. After grain refinement, there is a significant reduction in a crystallite size to ~ 100 nm by 1/2 HPT turn and it further decreased gradually to ~ 75 nm though 8 turns. With the grain refinement process, the microstrain significantly increased to ~ 0.0081 after 1/2 turn and remained reasonably constant though 8 HPT turns. It should be noted that the crystallite size calculated by XRD is often smaller than the actual grain size after severe plastic deformation processes due to the high populations of subgrains and dislocation walls [24,25] and crystallographic direction, measuring the coherent crystallite size. Nevertheless, the crystallite sizes computed using the XRD data are in good agreement with the grain sizes measured directly from the TEM micrographs as shown in Fig. 3(c) and (d) for the AM HEA after HPT.

The changes in the lattice parameter of the CoCrFeNi alloy through printing followed by grain refinement were calculated based on the positions of the diffraction peaks for all five plane coordinates using the XRD profile. The estimated lattice parameters are listed in Table 1 for the HEA in different processing conditions. The pre-alloyed powders having a lattice parameter of 3.572 \AA increases slightly after building, and grain refinement increased the value gradually towards 3.577 \AA through 8 HPT turns. This increase in lattice parameter may be partly attributed to the dissolution of the minority phases having larger lattice parameters during grain refinement by HPT. The phenomenon is well supported by the recent reports documenting the strong influence of dissolutions and supersaturation of the minority phases into a matrix phase on the XRD peak shifts by compositional straining during a solid-state reaction of Al and Mg by HPT [76,77]. Such expansion in lattice parameter was also shown in a two-phase CoCrFeMnNi alloy produced by HPT-driven mechanically alloying for 1, 10 and 100 turns, where the observed peak shifting between 1 turn and 10 turns involves the dissolution of a *b.c.c.* phase in an *f.c.c.* matrix phase, while additional large shifting of the *f.c.c.* peaks without any phase transformation may be due to an increase of microstrain by grain refinement through 10 to 100 HPT turns [31]. Thus, it is reasonable to anticipate that, beside the mechanical dissolution of the minority phases, there is a contribution of grain refinement to an increase of microstrain and expansion of the lattice parameter in the present AM CoCrFeNi alloy through HPT for 8 turns. The result is in good agreement with an earlier report evaluating theoretically the inherent correlation of microstrain and lattice parameter changes in nanocrystalline materials [78], where both microstrain and lattice parameter tend to increase exponentially with grain (crystallite) refinement, while there are always scatters due to the different grain boundary structures depending on the processing methods. Subsequently, the present study demonstrated the improvement in micro-mechanical properties and structural development in the AM CoCrFeNi HEA, and the results yield comprehensive knowledge of the advantages of grain refinement and structural changes for current development in the AM technology of HEAs.

5. Summary and conclusions

- (1) The importance of grain refinement in the micro-mechanical properties and structures of an AM CoCrFeNi HEA was examined after HPT for up to 8 turns under 6 GPa, and the results were compared with those acquired in a CM CoCrFeNi HEA after HPT through 5 turns.
- (2) A significant hardness increase was observed up to $\epsilon_{eq} \approx 12$ and thereafter the hardness saturated at $H_V = 525$ for both AM and CM HEA, while the initial hardness values before the grain refinement process were different due to the separate manufacturing preparations of the alloys. The AM HEA shows the

high strain hardening capability with a tendency of continuous increase in hardness with grain refinement even at $\epsilon_{eq} > 12$.

- (3) Grain refinement improved the strain rate sensitivity of the CoCrFeNi HEA, but the AM HEA demonstrated higher strain rate sensitivity of $m = 0.058$, thus high plasticity, than the CM HEA. Together with the high capability of strain hardening, excellent ductility is anticipated in the AM CoCrFeNi HEA. The estimated activation volume suggested the grain boundary-mediated dislocation activities as the rate-controlling mechanism of the AM HEA and it is consistent with the general nanocrystalline *f.c.c.* metals.
- (4) XRD analysis demonstrated grain refinement in the AM CoCrFeNi alloy reduced the crystallite size that is well correlated with an increase of microstrain and expansion of the lattice parameter by the combination of mechanical dissolution of the minority phases and severe grain refinement. The out-of-close-packed-plane reflections broaden overemphasized revealing smaller coherent crystal sizes due to interception by large numbers of dislocations and planar faulting that agrees with the estimated rate-controlling mechanism in the nanocrystalline AM HEA.

Data availability

The data that support the findings of this study are available from the corresponding author on reasonable request.

CRediT authorship contribution statement

Wenrui Zhao: Investigation, Formal analysis. **Jae-Kyung Han:** Investigation, Formal analysis. **Yulia O. Kuzminova:** Resources. **Stanislav A. Evlashin:** Resources. **Alexander P. Zhilyaev:** Investigation. **Alexander M. Pesin:** Investigation. **Jae-il Jang:** Investigation, Writing - review & editing. **Klaus-Dieter Liss:** Formal analysis, Writing - review & editing. **Megumi Kawasaki:** Supervision, Writing - original draft.

Declaration of competing interest

The authors declare that they have no known competing financial interests or personal relationships that could have appeared to influence the work reported in this paper.

Acknowledgements

This study was supported in part by the National Science Foundation of the United States under Grant No. DMR-1810343; in part by a grant of the Russian Science Foundation (project No. 20-69-46042) and by the Ministry of Science and Higher Education of the Russian Federation (Contract No. 075-15-2019-869); and in part by the National Research Foundation of Korea (NRF) grants funded by MSIT (No. 2020R1A2B5B01001446 and No. 2020R1A5A6017701).

References

- [1] B. Cantor, I.T.H. Chang, P. Knight, A.J.B. Vincent, Microstructural development in equiatomic multicomponent alloys, *Mater. Sci. Eng. A*. 375–377 (2004) 213–218.
- [2] J.-W. Yeh, S.-K. Chen, S.-J. Lin, J.-Y. Gan, T.-S. Chin, T.-T. Shun, C.-H. Tsau, S.-Y. Chang, Nanostructured high-entropy alloys with multiple principal elements: novel alloy design concepts and outcomes, *Adv. Eng. Mater.* 6 (2004) 299–303.
- [3] C.-Y. Hsu, J.-W. Yeh, S.-K. Chen, T.-T. Shun, Wear resistance and high-temperature compression strength of fcc CuCoNiCrAl_{0.5}Fe alloy with boron addition, *Metall. Mater. Trans. A* 35 A (2004) 1465–1469.
- [4] M.-H. Tsai, Physical properties of high entropy alloys, *Entropy* 15 (2013) 5338–5345.
- [5] M.-H. Tsai, J.-W. Yeh, High-entropy alloys: a critical review, *Mater. Res. Lett.* 2 (2014) 107–123.
- [6] E.J. Pickering, N.G. Jones, High-entropy alloys: a critical assessment of their founding principles and future prospects, *Int. Mater. Rev.* 61 (2016) 183–202.
- [7] D.B. Miracle, O.N. Senkov, A critical review of high entropy alloys and related concepts, *Acta Mater.* 122 (2017) 448–511.

- [8] B. Gludovatz, E.P. George, R.O. Ritchie, Processing, Microstructure and mechanical properties of the CrMnFeCoNi high-entropy alloy, *JOM* 67 (2015) 2262–2270.
- [9] E.P. George, W.A. Curtin, C.C. Tasan, High entropy alloys: a focused review of, *Acta Mater.* 188 (2020) 435–474.
- [10] Y. Zhang, T.T. Zuo, Z. Tang, M.C. Gao, K.A. Dahmen, P.K. Liaw, Z.P. Lu, Microstructures and properties of high-entropy alloys, *Prog. Mater. Sci.* 61 (2014) 1–93.
- [11] Y. Shi, B. Yang, P.K. Liaw, Corrosion-resistant high-entropy alloys: a review, *Metals* 7 (2017) 43.
- [12] P. Sathiyamoorthi, H.S. Kim, High-entropy alloys with heterogeneous microstructure: processing and mechanical properties, *Prog. Mater. Sci.* (In press) DOI: 10.1016/j.pmatsci.2020.100709.
- [13] C.C. Koch, Nanocrystalline high-entropy alloys, *J. Mater. Res.* 32 (2017) 3435–3444.
- [14] M. Vaidya, G.M. Muralikrishna, B.S. Murty, High-entropy alloys by mechanical alloying: a review, *J. Mater. Res.* 34 (2019) 664–686.
- [15] W. Li, P. Liu, P.K. Liaw, Microstructures and properties of high-entropy alloy films and coatings: a review, *Mater. Res. Lett.* 6 (2018) 199–229.
- [16] X.H. Yan, J.S. Li, W.R. Zhang, Y. Zhang, A brief review of high-entropy films, *Mater. Chem. Phys.* 210 (2018) 12–19.
- [17] R.Z. Valiev, R.K. Islamgaliev, I.V. Alexandrov, Bulk nanostructured materials from severe plastic deformation, *Prog. Mater. Sci.* 45 (2000) 103–189.
- [18] H. Shahmir, T. Mousavi, J. He, Z. Lu, M. Kawasaki, T.G. Langdon, Microstructure and properties of a CoCrFeNiMn high-entropy alloy processed by equal-channel angular pressing, *Mater. Sci. Eng. A.* 705 (2017) 411–419.
- [19] R. Zheng, J. Chen, W. Xiao, C. Ma, Microstructure and tensile properties of nanocrystalline (FeNiCoCu)_{1-x}Ti_xAl₃ high entropy alloys processed by high pressure torsion, *Intermetallics* 74 (2016) 38–45.
- [20] B. Schuh, F. Mendez-Martín, B. Völker, E.P. George, H. Clemens, R. Pippan, A. Hohenwarter, Mechanical properties, microstructure and thermal stability of a nanocrystalline CoCrFeMnNi high-entropy alloy after severe plastic deformation, *Acta Mater.* 96 (2015) 258–268.
- [21] D.-H. Lee, I.-C. Choi, M.-Y. Seok, J. He, Z. Lu, J.-Y. Suh, M. Kawasaki, T. G. Langdon, J.-i. Jang, Nanomechanical behavior and structural stability of a nanocrystalline CoCrFeNiMn high-entropy alloy processed by high-pressure torsion, *J. Mater. Res.* 30 (2015) 2804–2815.
- [22] H. Shahmir, J. He, Z. Lu, M. Kawasaki, T.G. Langdon, Effect of annealing on mechanical properties of a nanocrystalline CoCrFeNiMn high-entropy alloy processed by high-pressure torsion, *Mater. Sci. Eng. A.* 676 (2016) 294–303.
- [23] V. Maier-Kiener, B. Schuh, E.P. George, H. Clemens, A. Hohenwarter, Nanoindentation testing as a powerful screening tool for assessing phase stability of nanocrystalline high-entropy alloys, *Mater. Des.* 115 (2017) 479–485.
- [24] A. Heczcel, M. Kawasaki, J.L. Lábár, J.-i. Jang, T.G. Langdon, J. Gubicza, Defect structure and hardness in nanocrystalline CoCrFeMnNi high-entropy alloy processed by high-pressure torsion, *J. Alloys Compd.* 711 (2017) 143–154.
- [25] J. Gubicza, P.T. Hung, M. Kawasaki, J.-K. Han, Y. Zhao, Y. Xue, J.L. Lábár, Influence of severe plastic deformation on the microstructure and hardness of a CoCrFeNi high-entropy alloy: a comparison with CoCrFeNiMn, *Mater. Char.* 154 (2019) 304–314.
- [26] Y. Zhao, X. Wang, T. Cao, J.-K. Han, M. Kawasaki, J.-i. Jang, H.N. Han, U. Ramamurty, L. Wang, Y. Xue, Effect of grain size on the strain rate sensitivity of CoCrFeNi high-entropy alloy, *Mater. Sci. Eng. A.* 782 (2020) 139281.
- [27] J.S. Belo, S.C. Marques, A.V. Castilho, L.M. de Oliveira, R.A. Simão, D.S. dos Santos, Hydrogen diffusivity and interaction with Fe₂₀Mn₂₀Ni₂₀Co₂₀Cr₂₀ and Fe₂₂Mn₄₀Ni₃₀Co₆Cr₂ high-entropy alloys, *J. Alloys Compd.* 815 (2020) 152314.
- [28] A.V. Podolskiy, Y.O. Shapovalov, E.D. Tabachnikova, A.S. Tortika, M. A. Tikhonovskiy, B. Joni, E. Ódor, T. Ungar, S. Maier, C. Rentenberger, M. J. Zehetbauer, E. Schafner, Anomalous evolution of strength and microstructure of high-entropy alloy CoCrFeNiMn after high-pressure torsion at 300 and 77 K, *Adv. Eng. Mater.* 22 (2020) 1900752.
- [29] Q.H. Tang, Y. Huang, Y.Y. Huang, X.Z. Liao, T.G. Langdon, P.Q. Dai, Hardening of an Al_{0.3}CoCrFeNi high entropy alloy via high-pressure torsion and thermal annealing, *Mater. Lett.* 151 (2015) 126–129.
- [30] P.F. Yu, H. Cheng, L.J. Zhang, H. Zhang, Q. Jing, M.Z. Ma, P.K. Liaw, G. Li, R.P. Liu, Effects of high pressure torsion on microstructures and properties of an Al_{0.1}CoCrFeNi high-entropy alloy, *Mater. Sci. Eng. A.* 655 (2016) 283–291.
- [31] A. Kilmametov, R. Kulagin, A. Mazilkin, S. Seils, T. Boll, M. Heilmaier, H. Hahn, High-pressure torsion driven mechanical alloying of CoCrFeMnNi high entropy alloy, *Scripta Mater.* 158 (2019) 29–33.
- [32] M.T. Tsai, J.C. Huang, W.Y. Tsai, T.H. Chou, C.-F. Chen, T.H. Li, J.S.C. Jang, Effects of ultrasonic surface mechanical attrition treatment on microstructures and mechanical properties of high entropy alloys, *Intermetallics* 93 (2018) 113–121.
- [33] T. Fujieda, H. Shiratori, K. Kuwabara, T. Kato, K. Yamanaka, Y. Koizumi, A. Chiba, First demonstration of promising selective electron beam melting method for utilizing high-entropy alloys as engineering materials, *Mater. Lett.* 159 (2015) 12–15.
- [34] Y. Brif, M. Thomas, I. Todd, The use of high-entropy alloys in additive manufacturing, *Scripta Mater.* 99 (2015) 93–96.
- [35] S. Gorsse, C. Hutchinson, M. Gouné, R. Banerjee, Additive manufacturing of metals: a brief review of the characteristic microstructures and properties of steels, Ti-6Al-4V and high-entropy alloys, *Sci. Technol. Adv. Mater.* 18 (2017) 584–610.
- [36] X. Li, Additive manufacturing of advanced multi-component alloys: bulk metallic glasses and high entropy alloys, *Adv. Eng. Mater.* 20 (2018) 1700874.
- [37] S. Chen, Y. Tong, P.K. Liaw, Additive manufacturing of high-entropy alloys: a review, *Entropy* 20 (2018) 937.
- [38] C. Han, Q. Fang, Y. Shi, S.B. Tor, C.K. Chua, K. Zhou, Recent advances on high-entropy alloys for 3D printing, *Adv. Mater.* 32 (2020) 1903855.
- [39] J.M. Torralba, M. Campos, High entropy alloys manufactured by additive manufacturing, *Metals* 10 (2020) 639.
- [40] Z. Tong, H. Liu, J. Jiao, W. Zhou, Y. Yang, X. Ren, Microstructure, microhardness and residual stress of laser additive manufactured CoCrFeMnNi high-entropy alloy subjected to laser shock peening, *J. Mater. Process. Technol.* 285 (2020) 116806.
- [41] T.A. Listyawan, A. Kumar, W. Shin, H. Do, K.-H. Lee, J. Ryu, N. Park, Surface hardening treatment of Fe₄₀(CoCrMnNi)₆₀ medium entropy alloy via aerosol deposition technique: a new approach, *Mater. Lett.* 269 (2020) 127633.
- [42] P. Wang, P. Huang, F.L. Ng, W.J. Sin, S. Lu, M.L.S. Nai, Z.L. Dong, J. Wei, Additively manufactured CoCrFeNiMn high-entropy alloy via pre-alloyed powder, *Mater. Des.* 168 (2019) 107576.
- [43] Y. Kuzminova, D. Firsov, A. Dudin, S. Sergeev, A.P. Zhilyaev, A. Dyakov, A. Chupeeva, A. Alekseev, D. Martynov, I. Akhatov, S. Evlashin, The effect of the parameters of the powder bed fusion process on the microstructure and mechanical properties of CrFeCoNi medium-entropy alloys, *Intermetallics* 116 (2020) 106651.
- [44] C.L. Wang, Y.H. Lai, J.C. Huang, T.G. Nieh, Creep of nanocrystalline nickel: a direct comparison between uniaxial and nanoindentation creep, *Scripta Mater.* 62 (2010) 175–178.
- [45] A.P. Zhilyaev, T.G. Langdon, Using high-pressure torsion for metal processing: fundamentals and applications, *Prog. Mater. Sci.* 53 (2008) 893–979.
- [46] Z.G. Zhu, Q.B. Nguyen, F.L. Ng, X.H. An, X.Z. Liao, P.K. Liaw, S.M.L. Nai, J. Wei, Hierarchical microstructure and strengthening mechanisms of a CoCrFeNiMn high entropy alloy additively manufactured by selective laser melting, *Scripta Mater.* 154 (2018) 20–24.
- [47] S. Praveen, B.S. Murty, R.S. Kottada, Alloying behavior in multi-component AlCoCrCuFe and NiCoCrCuFe high entropy alloys, *Mater. Sci. Eng. A.* 534 (2012) 83–89.
- [48] R.B. Mane, B.B. Panigrahi, Sintering mechanisms of mechanically alloyed CoCrFeNi high-entropy alloy powders, *J. Mater. Res.* 33 (2018) 3321–3329.
- [49] D. Ma, M. Yao, K.G. Pradeep, C.C. Tasan, H. Springer, D. Raabe, Phase stability of non-equiatomic CoCrFeMnNi high entropy alloys, *Acta Mater.* 98 (2015) 288–296.
- [50] Z. Wang, Q. Wu, W. Zhou, F. He, C. Yu, D. Lin, J. Wang, C.T. Liu, Quantitative determination of the lattice constant in high entropy alloys, *Scripta Mater.* 162 (2019) 468–471.
- [51] C.L. Tracy, S. Park, D.R. Rittman, S.J. Zinkle, H. Bei, M. Lang, R.C. Ewing, W. L. Mao, High pressure synthesis of a hexagonal close-packed phase of the high-entropy alloy CrMnFeCoNi, *Nat. Commun.* 8 (2017) 15634.
- [52] Y. Akahama, M. Nishimura, K. Kinoshita, H. Kawamura, Y. Ohishi, Evidence of a fcc-hcp transition in aluminum at multimegabar pressure, *Phys. Rev. Lett.* 96 (2006), 045505.
- [53] M. Kawasaki, B. Ahn, P. Kumar, J.-i. Jang, T.G. Langdon, Nano- and micro-mechanical properties of ultrafine-grained materials processed by severe plastic deformation techniques, *Adv. Eng. Mater.* 19 (2017) 1600578.
- [54] Y. Zou, Nanomechanical studies of high-entropy alloys, *J. Mater. Res.* 33 (2018) 3035–3054.
- [55] E.O. Hall, The deformation and ageing of mild steel: II Characteristics of the Lüders deformation, *Proc. Phys. Soc. Sect. B.* 64 (1951) 742–747.
- [56] N.J. Petch, The cleavage strength of polycrystals, *J. Iron Steel Inst.* 174 (1953) 25–28.
- [57] B.S. Murty, J.W. Yeh, S. Ranganathan, High Entropy Alloys, Elsevier Science & Tech., Butterworth-Heinemann Ltd, Oxford, 2014.
- [58] M. Kawasaki, Different models of hardness evolution in ultrafine-grained materials processed by high-pressure torsion, *J. Mater. Sci.* 49 (2014) 18–34.
- [59] M. Kawasaki, R.B. Figueiredo, Y. Huang, T.G. Langdon, Interpretation of hardness evolution in metals processed by high-pressure torsion, *J. Mater. Sci.* 49 (2014) 6586–6596.
- [60] S.A. Torbati-Sarraf, S. Sabbaghianrad, R.B. Figueiredo, T.G. Langdon, Orientation imaging microscopy and microhardness in a ZK60 magnesium alloy processed by high-pressure torsion, *J. Alloys Compd.* 712 (2017) 185–193.
- [61] Y.C. Wang, T.G. Langdon, Effect of heat treatment on microstructure and microhardness evolution in a Ti-6Al-4V alloy processed by high-pressure torsion, *J. Mater. Sci.* 48 (2013) 4646–4652.
- [62] D. Hernández-Escobar, J. Marcus, J.-K. Han, R.R. Unocic, M. Kawasaki, C. J. Boehlert, Effect of post-deformation annealing on the microstructure and micro-mechanical behavior of Zn–Mg hybrids processed by high-pressure torsion, *Mater. Sci. Eng. A.* 771 (2020) 138578.
- [63] D. Tabor, Hardness of solids, *Rev. Phys. Technol.* 1 (1970) 145–179.
- [64] W.C. Oliver, G.M. Pharr, An improved technique for determining hardness and elastic modulus using load and displacement sensing indentation experiments, *J. Mater. Res.* 7 (1992) 1564–1583.
- [65] M. Shabani, J. Indeck, K. Hazeli, P.D. Jablonski, G.J. Pataky, Effect of strain rate on the tensile behavior of CoCrFeNi and CoCrFeMnNi high-entropy alloys, *J. Mater. Eng. Perform.* 28 (2019) 4348–4356.
- [66] W. Huo, F. Fang, X. Liu, S. Tan, Z. Xie, J. Jiang, Remarkable strain-rate sensitivity of nanotwinned CoCrFeNi alloys, *Appl. Phys. Lett.* 114 (2019) 101904.
- [67] J. Moon, S.I. Hong, J.B. Seol, J.W. Bae, J.M. Park, H.S. Kim, Strain-rate sensitivity of high-entropy alloys and its significance in deformation, *Mater. Res. Lett.* 7 (2019) 503–509.
- [68] F.D. Torre, P. Spätig, R. Schäublin, M. Victoria, Deformation behaviour and microstructure of nanocrystalline electrodeposited and high pressure torsioned nickel, *Acta Mater.* 53 (2005) 2337–2349.
- [69] Q. Wei, S. Cheng, K.T. Ramesh, E. Ma, Effect of nanocrystalline and ultrafine grain sizes on the strain rate sensitivity and activation volume: fcc versus bcc metals, *Mater. Sci. Eng. A.* 381 (2004) 71–79.

- [70] Z. Wu, Y. Gao, H. Bei, Thermal activation mechanisms and Labusch-type strengthening analysis for a family of high-entropy and equiatomic solid-solution alloys, *Acta Mater.* 120 (2016) 108–119.
- [71] T. Zhu, J. Li, A. Samanta, H.G. Kim, S. Suresh, Interfacial plasticity governs strain rate sensitivity and ductility in nanostructured metals, *Proc. Natl. Acad. Sci. U.S.A.* 104 (2007) 3031–3036.
- [72] H. Conrad, Grain size dependence of the plastic deformation kinetics in Cu, *Mater. Sci. Eng. A.* 341 (2003) 216–228.
- [73] H. Conrad, Plastic deformation kinetics in nanocrystalline fcc metals based on the pile-up of dislocations, *Nanotechnology* 18 (2007) 325701.
- [74] C. Niu, A.J. Zaddach, A.A. Oni, X. Sang, J.W. Hurt III, J.M. LeBeau, C.C. Koch, D. L. Irving, Spin-driven ordering of Cr in the equiatomic high entropy alloy NiFeCrCo, *Appl. Phys. Lett.* 106 (2015) 161906.
- [75] X. Li, R. Dippenaar, J.-K. Han, M. Kawasaki, K.-D. Liss, Phase transformation and structure evolution of a Ti-45Al-7.5Nb alloy processed by high-pressure torsion, *J. Alloys Compd.* 787 (2019) 1149–1157.
- [76] J.-K. Han, K.-D. Liss, T.G. Langdon, M. Kawasaki, Synthesis of a bulk nanostructured metastable Al alloy with extreme supersaturation of Mg, *Sci. Rep.* 9 (2019) 17186.
- [77] J.-K. Han, K.-D. Liss, T.G. Langdon, J.-i. Jang, M. Kawasaki, Mechanical properties and structural stability of a bulk nanostructured metastable aluminum-magnesium system, *Mater. Sci. Eng. A.* 796 (2020) 140050.
- [78] W. Qin, T. Nagase, Y. Umakoshi, J.A. Szpunar, Relationship between microstrain and lattice parameter change in nanocrystalline materials, *Phil. Mag. Lett.* 88 (2008) 169–179.